UNIVERSITÀ DEGLI STUDI DI PADOVA

UNIVERSITEIT GENT

Bayesian Inference of the 1D Electron Density Profile within the WEST Tokamak using Interferometry

by

Daniel Jordan

A masters thesis presented to the University of Padova
in fulfillment of the thesis requirement for the degree of
Physics of Data

The research was carried out at Ghent University with onsite supervison from
Geert Verdoolaege - Associate Professor
Hao Wu - PhD Student

Remote supervision from the university of Padova was provided by
Lidia Piron - Assistant Professor

2023

Author's Declaration

I hereby declare that I am the sole author of this thesis. This is a true copy of the thesis, including any required final revisions, as accepted by my examiners.

I understand that my thesis may be made electronically available to the public.

Abstract

The abstract should briefly highlight the importance of the research and present its key findings.

Acknowledgements

A big thank you to Hao Wu, Jeffry de Rycke, and Yangyang Zhang for their enlightening conversation and mentorship. I thank the rest of the team at infusion UGent, Geert Verdoolaege, Sven Van Loo, Jerome Alhage, Leonardo Caputo, and Joseph Hall for accepting me into their research group and including me in their research discussions. An extra thank you to Geert Verdoolaege for giving me this enriching opportunity.

Table of Contents

Author's Declaration ii

Abstract iii

Acknowledgements iv

List of Figures vii

1 Introduction 1

2 Background Theory of Bayesian Techniques and WEST Interferometry 2

2.1 The Tokamak 3

2.2 NICE 5

2.3 Bayesian Inference and Gaussian Process Regression 8

2.4 Interferometry and Polarimetry 13

2.5 Gaussian Process Regression for Interferometry 14

2.6 Chapter Summary 19

3 Methodology and Results 20

4 Conclusion 21

5 Future Investigation 22

References **23**

APPENDICES **25**

A Deriving the Closed Form Posterior Expressions **26**

B Deriving the Marginal Likelihood and Loss Function Expression **29**

C Complete Set of Distributions and Expressions for Reference **34**

C.1 Gaussian Process Regression for Interferometry, Discluding Artificial Observations 34

C.2 Gaussian Process Regression for Interferometry, Including Artificial Observations 36

Glossary **39**

List of Figures

2.1 A tokamak and relevant magnetic fields that create the helical particle trajectory [5]. . . . 3

2.2 Magnetic flux surfaces [9]. . . . 5

2.3 Electron density profile inferred by NICE for an instance in time within the WEST tokamak. . . . 7

2.4 Illustrating how many Gaussians can model a line and its uncertainty. . . . 9

2.5 A visualisation of the simple GPR process. . . . 10

2.6 The geometry of interfero-polarimetry lasers at WEST [3]. . . . 13

2.7 An example mesh grid to aid visualisation of the triangular mesh grid interpolation used in the response matrix construction. . . . 15

2.8 Hyperbolic tangent smooth step function for length scale, equation 2.22. Used to capture the drop at the edge of H-mode plasmas [1]. . . . 18

Chapter 1

Introduction

Introduce the main concepts, ideas and motivation. Include a small literature review on related works, including Newton direct and Inverse Computation for Equilibrium (NICE) and **Tungsten** (W) Environment in Steady-state Tokamak (WEST). Introduce the outline of the thesis.

Chapter 2

Background Theory of Bayesian Techniques and WEST Interferometry

This chapter aims to equip the reader with the necessary background theory required to reproduce this work and to understand the origin of the inferred electron density profiles presented in the results. It first describes a tokamak fusion device and some relevant physics concepts behind its function. It then describes in a high level manner the inference carried out by Blaise Faugeras and team with their code known as NICE [2]. After, the chapter outlines Bayesian inference and its connection with Gaussian Process Regression (GPR). Then the GPR method is explained in detail for a simple regression problem. Interferometry is introduced in enough detail that the GPR method can be altered to infer the electron density profile. The key factor is the new response matrix. Various options for advanced alterations are explained here and explored in the results section.

2.1 The Tokamak

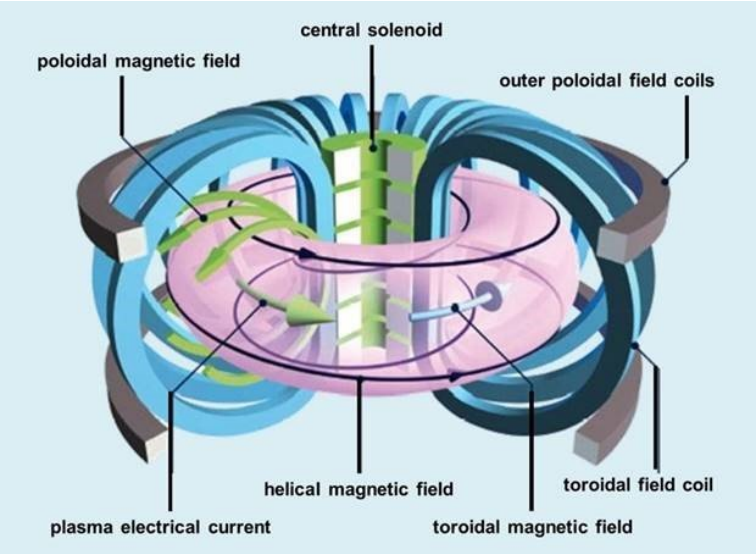

Figure 2.1: A tokamak and relevant magnetic fields that create the helical particle trajectory [5].

Tokamak is a class of fusion devices whose name comes from the abbreviation of a Russian phrase which means "toroidal chamber with magnetic coils". It consists of a doughnut shaped vacuum chamber surrounded by powerful magnets that aim to confine a high temperature plasma that would otherwise vaporise the chamber. The plasma pressure and temperature are fundamental parameters in the context of nuclear fusion because they dictate the conditions required to overcome the electrostatic repulsion between positively charged atomic nuclei and bring them close enough for the strong nuclear force to initiate fusion reactions. In the core of stars like our Sun, the immense pressure and temperature generated by the gravitational collapse create the conditions where hydrogen nuclei (protons) can overcome their natural repulsion and fuse into helium, releasing a tremendous amount of energy in the process. To initiate fusion, hydrogen must be heated to temperatures in the range of tens of millions of degrees Celsius. In a tokamak, this is mainly accomplished with ohmic heating via a driving plasma current and neutral gas injection. This involves accelerating hydrogen ions to high speeds with electric fields and neutralising them the instant before they enter the chamber. The resulting plasma attains the required temperature, allowing nuclei to collide with sufficient energy for fusion reactions

to occur. Figure 2.1 shows the position of various magnetic field coils within the tokamak. The toroidal magnetic field exerts an inward force on the plasma thus raising its pressure. High pressure is required to increase the frequency of collisions so that the energy output can exceed the large heating energy input. The central solenoid induces a current in the plasma which produces the majority of the poloidal magnetic field. This field is essential for confinement but it also plays a key role in plasma stability. The outer poloidal field coils can be controlled in real time to help mitigate instabilities. A real time inference of the electron density profile would assist in identifying instabilities and informing the algorithm that drives the control coils to mitigate them. In addition to high temperature and pressure, the tokamak design seeks to maximize the confinement time of the plasma. This is essential to allow a sufficient number of fusion reactions to occur before the plasma cools down or loses its stability. The magnetic fields in a tokamak are carefully optimized to prevent rapid plasma loss and minimize heat loss through various mechanisms, including turbulent transport. The shape of the density profile has a large effect on the confinement time.

The combination of the toroidal and poloidal fields shown in figure 2.1 creates a helical magnetic field within the plasma. Electrons and ions are accelerated in opposite toroidal directions by the central solenoid yet both follow a trajectory along the magnetic field lines. This is because a charged particle moving across a magnetic field succumbs to a force perpendicular to its motion. This causes them to gyrate around the magnetic field lines and confines them to follow the magnetic field lines. This is an oversimplification although a detailed description of particle motion within a magnetic field is not needed for this thesis. It is enough to know that if a single charged particle was within a tokamak then it would perfectly follow a trajectory along the helical path of the magnetic field lines with a small gyration around the field line. When many particles are introduced collisions can interrupt these trajectories, yet in many models used for data analysis the assumption that particles follow the magnetic field lines is used, including within this thesis.

The magnetic field lines are confined to magnetic flux surfaces, figure 2.2. The toroidal and poloidal flux is constant on magnetic flux surfaces, there is 0 flux across magnetic flux surfaces. Since we assume that the particles follow the magnetic field lines which are strictly bound to these surfaces, we also assume that the density is constant on these surfaces. This allows the density of the entire cross-section to be expressed with a 1D profile as a function of normalised radius ρ for example, see NICE's profile, figure 2.3. Where ρ is 0 at the plasma core and 1 at the edge. At the core the poloidal magnetic flux is maximum and the edge is the last closed flux surface. Particles past the edge are no longer bound and may interact with the plasma wall. The existence of nested magnetic flux surfaces shown in figure 2.2 rely on the ideal magnetohydrodynamics (MHD) assumptions.

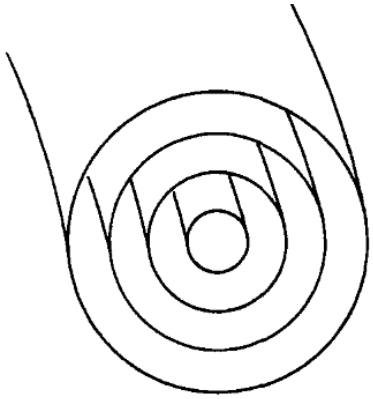

Figure 2.2: Magnetic flux surfaces [9].

Experiments frequently discover magnetic islands which discredits the assumption of nested flux surfaces. The electron density profiles inferred by NICE and this work make the nested flux surface assumption, although for many applications such as real time control, a highly accurate inference is often not required.

2.2 NICE

NICE is an equilibrium reconstruction code developed for the WEST tokamak. It is relevant because it computes an inference of the electron density profile that is available for comparison to the profile inferred in this work, although NICE's main objective is to infer the shape and position of the magnetic flux surfaces. NICE uses magnetic diagnostics. At WEST these include 421 pickup coils, 36 flux loops and 12 Rogowski coils [7]. Magnetic diagnostics provide the majority of the information. NICE also uses interferometry, polarimetry, motional stark effect and pressure measurements. Equation 2.10 and 2.11 further in the chapter, show how interferometry and polarimetry together can provide information about the poloidal magnetic field, which directly affects the magnetic flux and thus magnetic flux surfaces. NICE performs the inference by minimising a cost function. The cost function determines how well a physical state of the system matches the data received. A state is a specific position and shape of the magnetic flux surfaces and electron density profile. This requires a forward model. The forward model takes a state of the system and attempts to compute the signals that would be received by error free diagnostics if that state was the ground truth. The forward model is a simplified mathematical representation of the measurement process and can never be 100% accurate. This introduces errors in

the inference that need to be accounted for. The signals from the forward model can be compared to the actual signals received by the diagnostics to compute the cost function. By minimising the cost function the state that best matches the data is found. NICE uses Sequential Quadratic Programming (SQP) as the minimisation algorithm. The optimal state of the system is then stored in the Integrated Modeling and Analysis Suite (IMAS) database for WEST. This includes the 1D electron density profile used as a comparison for the profile inferred in this work. NICE also imposes regularisation terms on their cost function. These penalise the cost function when state properties have features that disagree with prior knowledge. This includes smoothness. We expect the magnetic flux surfaces and electron density profile, to be continuous and smooth. A state inputted into the cost function that is not smooth triggers the regularisation term which causes the cost function to be larger. Minimising the cost function now also leads to smooth magnetic flux surfaces and electron density profile. This leads to a difficult question, how smooth should it be? They also have a regularisation term to penalise the cost function if the electron density profile is far from 0 at the last closed flux surface or plasma edge. It is prior knowledge that the electron density is near 0 at the plasma edge. How close to 0, and how strong should the regularisation be is still an open question. This work's GPR approach has direct analogues to these regularisation terms. As explained later in more detail the length scale controls smoothness and an artificial observation ensures the density is close to zero at the edge. Figure 2.3 shows an example of a NICE inferred electron density profile. It is modelled with a cubic spline function. It is the parameters of the cubic spline that are inputted into the cost function. The errors are calculated using a sensitivity method. In short, the error is deemed larger for the electron density of a particular normalised radius if a large change in the density leads to a small change in the cost function. In this case, we cannot be certain what density is more true because many lead to a similarly low cost function and thus match the data similarly well. To include some more details, the SQP minimisation algorithm computes the hessian of the cost function for minimisation, but this hessian can also be used to measure the sensitivity and thus the errors. The diagonal of the hessian contains the second differential of the cost function for each input parameter. This describes the curvature of the cost function in the direction of each parameter. A smaller curvature means a smaller sensitivity and thus a larger error.

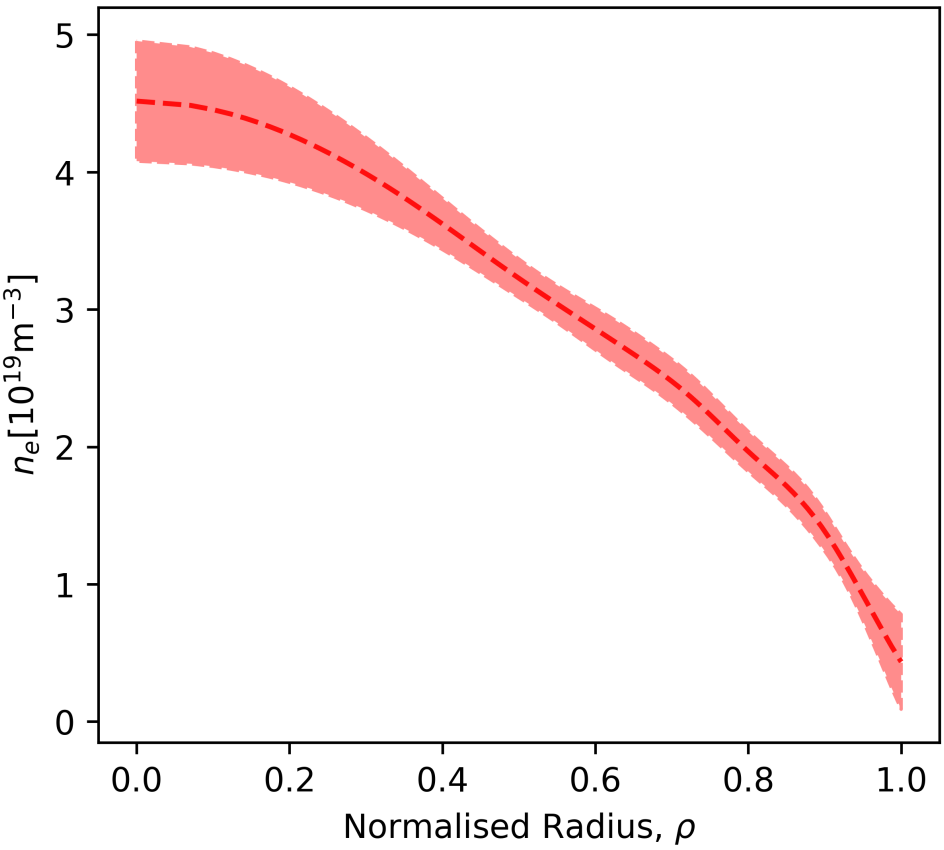

Figure 2.3: Electron density profile inferred by NICE for an instance in time within the WEST tokamak.

2.3 Bayesian Inference and Gaussian Process Regression

This work aims to use Bayesian inference to obtain the electron density profile. Bayes theorem for a physical quantity of interest q is expressed as,

$$P(q|D,I) = \frac{P(D|q,I)P(q|I)}{P(D|I)}, \tag{2.1}$$

the posterior $P(q|D,I)$ is the probability density distribution of q given the measured data D and some prior information I. The maximum of the posterior is the most probable value of q given the data and prior information. The uncertainty of q can also be obtained from the posterior. The likelihood $P(D|q,I)$ is the probability density function that expresses the probability of the measured data given a fixed value of q and the prior information. The likelihood is described by the experimental error for the data collection. The prior $P(q|I)$ contains information assumed about q before the data is taken. The marginal likelihood or evidence $P(D|I)$ is simply the probability of the data given the prior information only. For posterior computation, the marginal likelihood serves as a normalisation factor. Normalisation is often carried out with other means to simplify the posterior computation. Although the marginal likelihood can be used to tune hyperparameters. For example, the degree or strength of prior information is uncertain and by finding the strength that maximises the marginal likelihood we find the prior that matches the data the best. Maximising the marginal likelihood to tune the hyperparameters also aids in avoiding over-fitting, as the trade off between model complexity and data-fit is automatic via Occam's razor principle [6]. The marginal likelihood method is powerful although it is important to remember that it is not perfect and does not guarantee to find the hyperparameters that lead to the most accurate posterior.

GPR is a form of Bayesian inference where we assume these distributions can be expressed with multivariate Gaussian distributions. When the prior and posterior have the same form then the prior is known as a conjugate prior. This simplifies the inference as it is possible to find a closed form expression of the posterior. Without a closed form expression, the posterior must be approximated with sampling techniques. GPR is the technique used in this work to infer the electron density profile from interferometry data. First, the technique is introduced for a simple regression problem where we wish to fit a curve to a set of points.

A multivariate Gaussian can be used to model a curve and its uncertainty, as illustrated in the violin plot of figure 2.4. The functional form of a multivariate Gaussian is,

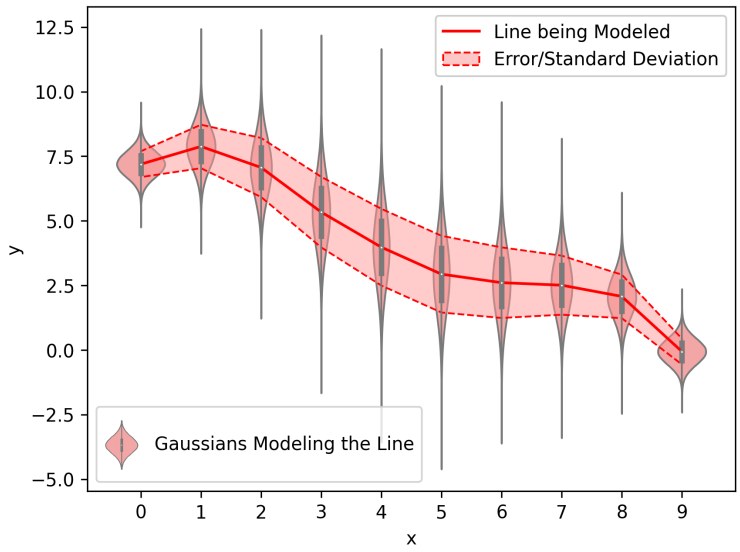

Figure 2.4: Illustrating how many Gaussians can model a line and its uncertainty.

$$\mathcal{N}(\vec{y}, \vec{\mu}, \Sigma) = \frac{1}{\sqrt{(2\pi)^{\frac{n}{2}}|\Sigma|}} \exp\left[-\frac{1}{2}(\vec{y}-\vec{\mu})^T\Sigma^{-1}(\vec{y}-\vec{\mu})\right], \tag{2.2}$$

the mean vector $\vec{\mu}$ holds the y values of the curve at regular intervals along the x axis. The diagonal of the covariance matrix holds the standard deviations of each Gaussian within the multivariate. These represent the errors of the curve. Figure 2.4 shows 10 Gaussians but in practice many are used to ensure a smooth curve. In this way, a multivariate Gaussian can be used to represent the curve resulting from GPR.

The simple regression problem consists of points to which one would like to fit a smooth curve. To solve this using GPR one must define the likelihood and prior as multivariate Gaussians. If m measurements are taken the likelihood is

$$\mathcal{N}(\vec{d}, \vec{\mu}_{li} = R\vec{y}, \Sigma_{li}), \qquad \Sigma_{li} = \vec{\epsilon}I = \begin{bmatrix} \epsilon_1 & 0 & \dots & 0 \\ 0 & \epsilon_2 & \dots & 0 \\ \vdots & \vdots & \ddots & 0 \\ 0 & 0 & 0 & \epsilon_m \end{bmatrix}, \tag{2.3}$$

and the prior is

$$\mathcal{N}(\vec{y}, \vec{\mu}_{pr} = \vec{0}, K), \qquad K_{ij} = k(y_i, y_j) = \sigma \exp\left[\frac{y_i - y_j}{2l^2}\right]. \tag{2.4}$$

The goal is to compute the posterior,

$$\mathcal{N}(\vec{y}, \mu_{\vec{post}}, \Sigma_{post}), \tag{2.5}$$

which represents the best fit given the data. The many Gaussians that make up these multivariate Gaussians are visualised in figure 2.5.

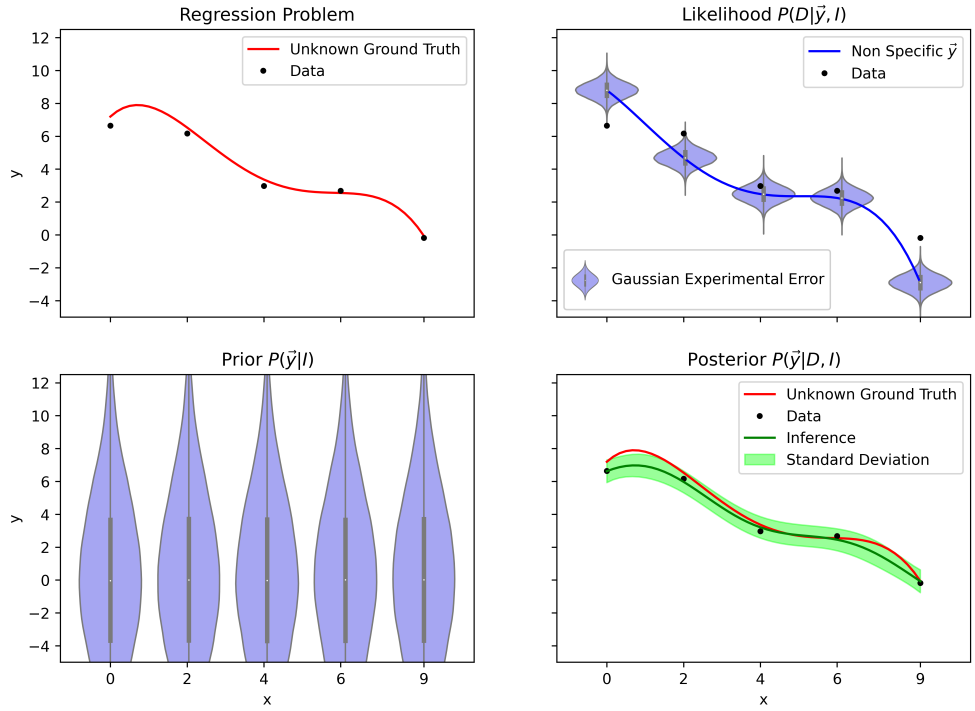

Figure 2.5: A visualisation of the simple GPR process.

This visualisation aid is helpful to appreciate the role of the likelihood and prior but it is not always a perfect representation. The likelihood has a diagonal covariance matrix and so the multiple Gaussians that make up the likelihood are not dependent on each other, thus representing them individually provides all the information in the likelihood. The prior has a more complex covariance matrix K, and figure 2.5 does not have a complete

representation of the priors form. To compute the posterior in figure 2.5 one must understand the components of the posterior, likelihood, prior and how they can be combined into the closed form equations. Starting with the posterior, equation 2.5, $\vec{y}$ contains the random variables y_i for regularly spaced positions x_i. Given the data the most probable values of $\vec{y_i}$ are in $\vec{\mu_{post}}$ and their uncertainties in the diagonal of Σ_{post}. In the likelihood, equation 2.3, $\vec{d}$ is the data vector containing all the y-values from measurements at various x positions. R is known as the response matrix and ensures that the mean vector of the likelihood $R\vec{y}$ only contains values of $\vec{y}$ at the same x positions the data was recorded at. R is essentially a filter that removes irrelevant y_i values from $\vec{y}$ for the mean vector of the likelyhood. This ensures the mean vector has the same length as the data vector. In the likelihood of figure 2.5 you can see an example of a given $\vec{y}$ and the mean of each Gaussian is the value on that line at the same x position as the data point. $\vec{\epsilon}$ contains the experimental error of the measurements in $\vec{d}$. In the prior, equation 2.4, there are as many Gaussians as in the posterior but each of these Gaussians has a mean of 0. The $\vec{0}$ symbol represents a vector of zeros the same length as the vector $\vec{y}$ of random variables. To aid visualisation the prior in figure 2.5 only shows 5 out of the 101 Gaussians used. The covariance matrix K is constructed using the kernel $k(x_i, x_j)$. The main role of the amplitude, σ, in the kernel is to set the prior strength. The length scale, l sets the strength of the correlation of neighbouring Gaussians. A low length scale means that only Gaussians close in x are highly correlated. Gaussians further in x would have a low correlation, meaning they can have a very different mean value. A low length scale allows the fitted curve to have more complexity similar to a high order polynomial and can lead to overfitting. A high length scale limits the fit's ability to curve sharply leading to a simple model, similar to a low order polynomial, leading to underfitting. A very high length scale leads to an almost linear fit, every time. This prior is far from perfect. For instance, it is often known that the inferred values must be positive, for example, you cannot have a negative electron density. Since the prior mean vector is set to $\vec{0}$, a negative value is as likely to be inferred as a positive value. Since it is Gaussian, values close to 0 are more likely to be inferred than values far from 0. To mitigate this a high amplitude can be used to lower the prior strength and allow the data in the likelihood to have more influence on the posterior result. The kernel $k(x_i, x_j)$ in equation 2.4 is known as the static exponential square kernel. It is a very commonly used kernel in GPR but far from the only choice. The single value of the length scale prevents the inference from having long smooth regions with few features followed by regions of high variability. This can be an issue when inferring H-mode tokamak plasmas that have a sharp drop-off in density at the edge. For these situations, a non-static kernel can be used that allows the length scale to be a function of x which can then allow for posteriors of varying complexity. Regardless of the kernel used, deciding

the optimal values of its parameters for a problem is not obvious. A common solution is to use the marginal likelihood of equation 2.1 as a loss function. The parameters that maximise it can be found with gradient based methods. This finds the parameters that maximise the probability of the data being measured. Although the marginal likelihood method is also known for automatically deploying Occam's razor principle which finds a balance between closely fitting the data and having a simple model that accounts for the data's errors to have a more accurate inference [6] [8]. Essentially maximising the marginal likelihood avoids overfitting. Although this method is powerful it does not guarantee to produce parameters that lead to the most accurate fit. To get a more accurate fit, bayesian sampling techniques can be used, although this is more computationally expensive.

The posterior mean vector and covariance matrix can be expressed by the closed form expressions,

$$\vec{\mu}_{post} = \vec{\mu}_{pr} + (K^{-1} + R^\top \Sigma_{li}^{-1} R)^{-1} R^\top \Sigma_{li}^{-1} (\vec{d} - R\vec{\mu}_{pr}), \tag{2.6}$$

$$\Sigma_{post} = \left(R^\top \Sigma_{li}^{-1} R + K^{-1}\right)^{-1}, \tag{2.7}$$

these are derived in appendix A. The main steps include multiplying the functional forms of the prior and likelihood, ignoring all scaling factors, simplifying until they form a single unnormalised multivariate Gaussian and then comparing this with the posterior. The marginal likelihood can be expressed as,

$$\begin{aligned} P(\vec{d}|\vec{\epsilon},\theta) &= \int P(\vec{d}|\vec{y},\vec{\epsilon}) P(\vec{y}|\theta)\, d\vec{y} \\ &= \frac{1}{(2\pi)^{\frac{m}{2}} \sqrt{|\Sigma_{li} + RKR^\top|}} \exp\left[-\frac{1}{2}(\vec{d} - R\vec{\mu}_{pr})^\top (\Sigma_{li} + RKR^\top)^{-1} (\vec{d} - R\vec{\mu}_{pr})\right]. \end{aligned} \tag{2.8}$$

The values of the marginal likelihood can become very large and troublesome to compute with standard 64-bit float precision. For this reason, the logarithm is computed. It is the convention when performing optimisation to define a loss function to be minimised, thus the negative log marginal likelihood is used. Scaling constants do not affect the minimum value and can be ignored. The negative log marginal likelihood used as a loss function for hyper-parameters is then,

$$-\ln(P(\vec{d}|\vec{\epsilon},\theta)) \propto \ln(|\Sigma_{li} + RKR^\top|) + (\vec{d} - R\vec{\mu}_{pr})^\top (\Sigma_{li} + RKR^\top)^{-1} (\vec{d} - R\vec{\mu}_{pr}), \tag{2.9}$$

the full derivation of this expression can be found in appendix B.

2.4 Interferometry and Polarimetry

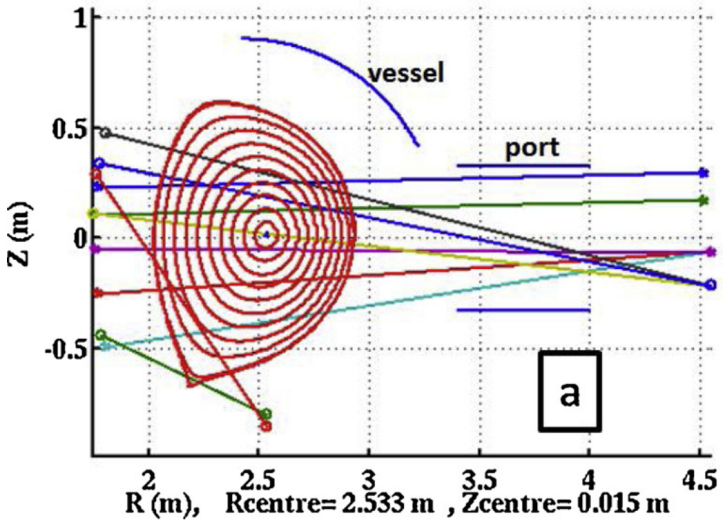

Figure 2.6: The geometry of interfero-polarimetry lasers at WEST [3].

Both Interferometry and polarimetry gain information from the same lasers. The lasers are fired through the plasma at multiple angles. The geometry at WEST is shown in figure 2.6. The refractive index of the plasma is dependent on the electron density. The lasers slow and the phase shift can be measured with interferometry. This phase shift is proportional to the line integrated electron density n_e along the line of sight of the lasers,

$$\Delta\phi = \frac{\lambda e^2}{4\pi\epsilon_0 m_e c^2} \int n_e \, dl \, [4], \tag{2.10}$$

The laser wavelength λ, is combined with other common physical constants to ascertain the constant of proportionality. WEST has stored the line integrated electron density as raw interferometry data in the IMAS database. This is the data that will be used for this work.

Polarimetry measures the Faraday rotation angle of the lasers. The linearly polarised lasers experience a rotation as the circularly polarised components travel through the

plasma at different speeds. This is due to the small gyration of the electrons around the magnetic field. The Faraday rotation angle is proportional to the line integrated density of $n_e B_{||}$ along the line of sight of the lasers,

$$\theta_F = \frac{\lambda^2 e^3}{8\pi^2 c^3 \epsilon_0 m_e^2} \int n_e B_{||} \, dl \, [4], \tag{2.11}$$

where $B_{||}$ is the magnetic field strength parallel to the line of sight. Polarimetry has information about electron density and this work could be extended to become a Bayesian integrated analysis which includes this information in the inference. Currently only interferometry information is used. Polarimetry can be used in combination with interferometry to gain information about the poloidal magnetic field and this is why NICE uses it to determine the position of the magnetic flux surfaces.

2.5 Gaussian Process Regression for Interferometry

To infer the electron density profile with interferometry the GPR process is altered. $\vec{y}$ becomes $\vec{n_e}$, the $\vec{0}$ prior mean can remain the same. The amplitude σ and length-scale l can be re-optimised by maximising the marginal likelihood. The data is now in a different space and thus is the likelihood. The response matrix R must be created so that it will transform a profile $\vec{n_e}$ into what would be measured by an error free version of the WEST interferometry system given $\vec{n_e}$ is the true profile. The result of $R\vec{n_e}$ is a vector the same length as the data $\vec{d}$ where each element corresponds to a different interferometry laser or channel.

The response matrix computation can be summarised in a few steps. NICE provides the magnetic flux at a set of grid points on the tokamak cross-section. It also provides the flux at a set of flux surfaces of known normalised radius ρ. A simple 1D interpolation can be used to determine the normalised radius at each grid point. Then using $\vec{n_e}$ another 1D interpolation can be done to determine the electron density at each grid point. After the density at any point along a laser's line of sight can be computed using triangular mesh interpolation. The density at the golden cross in figure 2.7 can be computed as a weighted sum of the three nearest known density points that form the golden triangle,

$$n_e(l_i) = \lambda_1 n_e(g_1) + \lambda_2 n_e(g_2) + \lambda_3 n_e(g_3), \tag{2.12}$$

where λ values can be computed using the $(R_1, z_1), (R_2, z_2), (R_3, z_3)$ coordinates of the 3 known density points and the point of interest (R, z),

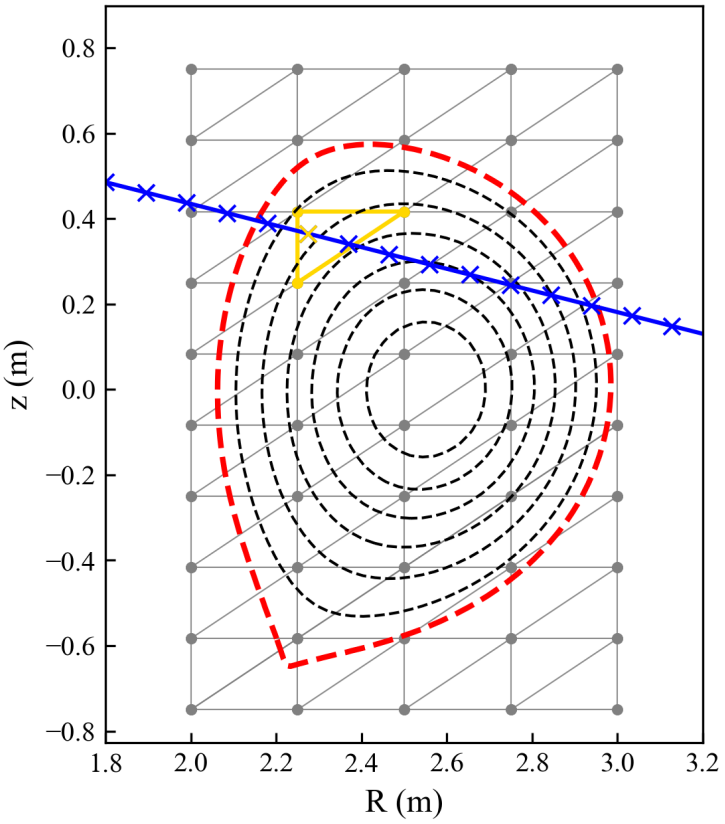

Figure 2.7: An example mesh grid to aid visualisation of the triangular mesh grid interpolation used in the response matrix construction.

$$\lambda_1 = \frac{(z_2 - z_3)(R - R_3) + (R_3 - R_2)(z - z_3)}{(z_2 - z_3)(R_1 - R_3) + (R_3 - R_2)(z_1 - z_3)}, \tag{2.13}$$

$$\lambda_2 = \frac{(z_3 - z_1)(R - R_3) + (R_1 - R_3)(z - z_3)}{(z_2 - z_3)(R_1 - R_3) + (R_3 - R_2)(z_1 - z_3)}, \tag{2.14}$$

$$\lambda_3 = 1 - \lambda_1 - \lambda_2, \tag{2.15}$$

these λ values are known as the barycentric coordinates of the point of interest. The line integrated density can be approximated as a sum of electron densities at many points along the line of sight times the width of their separation,

$$\int n_e \, dl \approx \sum_i n_e(l_i) \Delta l. \tag{2.16}$$

The contribution $w(g_i)$ of each grid point g_i is a sum of all the mesh interpolation coefficiants λ_j used on that point,

$$\int n_e \, dl \approx \Delta l \sum_i w(g_i) n_e(g_i), \; w(g_i) = \sum_j \lambda_j. \tag{2.17}$$

Each point can be associated with the nearest flux surface f_i equally spaced in ρ. This way the contribution $w(f_i)$ of each flux surface is a sum of the contribution at each of its associated grid points g_j,

$$\int n_e \, dl \approx \Delta l \sum_i w(f_i) n_e(f_i), \; f = \sum_j g_j. \tag{2.18}$$

All of these steps equate to a simple re-ordering of the original summation 2.16 to extract the contribution of each flux surface on the final integrated density value. Equation 2.18 can be computed using a vector product,

$$\int n_e \, dl \approx \Delta l \vec{w}^\top \vec{n_e}. \tag{2.19}$$

The contribution vector applies to one line of sight. The computation for all lines of sight can be performed by placing the $\Delta l \vec{w}$ vector for each line of sight as a row in the response matrix R. Thus, a vector of line integrated densities for the likelihood can be created,

$$\vec{\mu_{li}} = R\vec{n_e}. \tag{2.20}$$

This responce matrix R can then be used in the closed form expressions 2.6 and 2.7, to perfrom a 1D electron density profile inference.

Some further alterations to the GPR method can be made to further increase the reliability of the inference. These include altering the kernel and adding artificial observations to include prior knowledge. The kernel can be changed to a non-static kernel,

$$K_{ij} = k(\rho_i, \rho_j) = \sigma^2 \left(\frac{2l(\rho_i)l(\rho_j)}{l(\rho_i)^2 + l(\rho_j)^2} \right)^{1/2} \exp\left(\frac{(\rho_i - \rho_j)^2}{l(\rho_i)^2 + l(\rho_j)^2} \right), \tag{2.21}$$

this allows the length scale to change as a function of ρ. The length scale controls smoothness, model complexity and curvature. If these are free to change for different regions of the plasma then there is a greater range of possibilities for the final inference. Chilenski used a hyperbolic tangent function,

$$l(\rho) = \frac{l_{core} + l_{edge}}{2} + \frac{l_{core} - l_{edge}}{2} \tanh\left(\frac{\rho - \rho_{step_center}}{\rho_{step_width}} \right) \text{ [1]}, \tag{2.22}$$

to form a smooth step down from a high length scale at the core to low at the edge, see figure 2.8. The extra freedom at the edge allows the inference to accommodate for a large sudden drop in electron density, which is a common feature for H-mode plasmas. H-mode plasmas are known to have a longer confinement time and thus better fusion performance. WEST does not operate in H-mode, although this method is tested with synthetic data from a simple H-mode simulation.

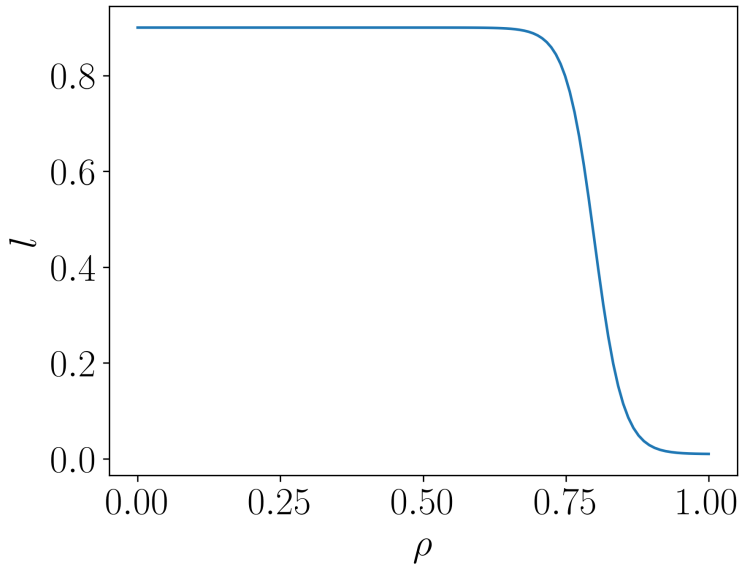

Figure 2.8: Hyperbolic tangent smooth step function for length scale, equation 2.22. Used to capture the drop at the edge of H-mode plasmas [1].

Traditionally prior information should be included in the prior distribution. However, in practice precision errors can make this difficult in the GPR framework and it is often more convenient to place prior information into the likelihood in the form of artificial observations. This method was also adopted by Chilenski [1]. The density is known to be close to 0 at the edge, ($\rho = 1$). It is also known that the density profile is smooth and symmetric meaning the gradient of the profile at the core must be close to 0. The point of reflection for the symmetry is the core. This information can be included in the data, $\vec{d}$, with an artificial experimental error determining the strength of the information included in $\vec{\epsilon}$. Other parts of the GPR method need to be altered to accommodate the new information. The vector to be infered $\vec{a}$ is not only $\vec{n_e}$ but also includes $n_e(\rho = 1)$ and $n'_e(\rho = 0)$ concatonated onto the end. This allows the response matrix alteration to be simple,

$$R^{alt} = \begin{bmatrix} R & \cdots & 0 & 0 \\ \vdots & \ddots & 0 & 0 \\ 0 & 0 & 1 & 0 \\ 0 & 0 & 0 & 1 \end{bmatrix}. \tag{2.23}$$

The prior covariance matrix must also be altered. The covariance between a gradient and non-gradient data point is simply the differential of the covariance over the gradient data point. For two gradient data points, it is a differential over each point.

$$K'_{ij} = k'(\rho_i, \rho_j) = \frac{\partial k'(\rho'_i, \rho_j)}{\partial \rho'_i} \text{ [1]}, \tag{2.24}$$

$$K''_{ij} = k''(\rho'_i, \rho'_j) = \frac{\partial k''(\rho'_i, \rho'_j)}{\partial \rho'_i \partial \rho'_j} \text{ [1]}. \tag{2.25}$$

In this notation ρ' indicates the position of a gradient data point. The alternate kernel is then,

$$K^{alt} = \begin{matrix} K & K' \\ -K'^{\top} & K''. \end{matrix} \tag{2.26}$$

The necessary adaptations for GPR to Interferometry have been described. For reference, the various final distributions and expressions after the adaptations are fully shown in appendix C.

2.6 Chapter Summary

The electron density profile is important as it plays a key role in determining the energy confinement time and informing real time control systems. With the assumption of magnetic flux surfaces, one can express it as a 1D profile. NICE is an equilibrium reconstruction code that also infers the electron density profile that can be used as a comparison in this thesis. GPR is a form of Bayesian inference that can be applied to interferometry data to infer the electron density profile. A non-static kernel can be used to allow the inference to have a model complexity that varies with ρ. Hyperparameters can be tuned by minimising the negative log marginal likelihood. Prior information can be easily included in the likelihood with artificial observations. In the results section, these methods will be deployed on synthetic data. The inference performance can be determined by how closely it fits the ground truth profile. They will also be deployed on real WEST data and the results will be compared to that obtained by NICE.

Chapter 3

Methodology and Results

Chapter 4

Conclusion

The conclusion should have a short summary of each chapter highlighting the main parts of a story from data to inference to insights. Lead into future investigations.

Chapter 5

Future Investigation

References

[1] M.A. Chilenski, M. Greenwald, Y. Marzouk, N.T. Howard, A.E. White, J.E. Rice, and J.R. Walk. Improved profile fitting and quantification of uncertainty in experimental measurements of impurity transport coefficients using gaussian process regression. *Nuclear fusion*, 55(2):23012–20, 2015.

[2] Blaise Faugeras. An overview of the numerical methods for tokamak plasma equilibrium computation implemented in the nice code. *Fusion engineering and design*, 160:112020–, 2020.

[3] C. Gil, G. Colledani, M. Domenes, D. Volpe, A. Berne, F. Faisse, C. Guillon, J. Morales, P. Moreau, and B. Santraine. Renewal of the interfero-polarimeter diagnostic for west. *Fusion engineering and design*, 140:81–91, 2019.

[4] Ian H. Hutchinson and Ian H. Hutchinson. *Principles of plasma diagnostics / I. H. Hutchinson*. Cambridge University press, Cambridge etc, c1987.

[5] S. Li, H. Jiang, Z. Ren, and C. Xu. Optimal tracking for a divergent-type parabolic pde system in current profile control. *Abstract and applied analysis*, 2014:1–8, 2014.

[6] David J.C. MacKay. *Bayesian methods for adaptive models*. PhD thesis, California Institute of Technology, 1992.

[7] P. Moreau, A. Le-Luyer, P. Spuig, P. Malard, F. Saint-Laurent, J. F. Artaud, J. Morales, B. Faugeras, H. Heumann, B. Cantone, M. Moreau, C. Brun, R. Nouailletas, E. Nardon, B. Santraine, A. Berne, P. Kumari, and S. Belsare. The new magnetic diagnostics in the west tokamak. *Review of scientific instruments*, 89(10):10J109–10J109, 2018.

[8] Carl Edward. Rasmussen and Christopher K. I. Williams. *Gaussian processes for machine learning*. Adaptive computation and machine learning. MIT Press, Cambridge, Mass, 2006.

[9] John Wesson and John Wesson. *Tokamaks / John Wesson ; with contributions from D.J. Campbell et al.* The Oxford engineering science series. Clarendon Press, Oxford, 2. ed edition, 1997.

APPENDICES

/

Appendix A

Deriving the Closed Form Posterior Expressions

The inference begins with Bayes theorem,

$$P(\vec{y}|\vec{d},\vec{\epsilon},\theta) = \frac{P(\vec{d}|\vec{y},\vec{\epsilon})P(\vec{y}|\theta)}{P(\vec{d}|\vec{\epsilon},\theta)}, \tag{A.1}$$

where the likelihood can be written as,

$$P(\vec{d}|\vec{y},\vec{\epsilon}) = \frac{1}{(2\pi)^{\frac{m}{2}}\sqrt{|\Sigma_{li}|}} \exp\left[-\frac{1}{2}(\vec{d}-R\vec{y})^{\top}\Sigma_{li}^{-1}(\vec{d}-R\vec{y})\right],\ \Sigma_{li} = \vec{\epsilon}I, \tag{A.2}$$

the prior as,

$$\begin{aligned} P(\vec{y}|\theta) &= \frac{1}{(2\pi)^{\frac{n}{2}}\sqrt{|K|}} \exp\left[-\frac{1}{2}(\vec{y}-\vec{\mu}_{pr})^{\top}K^{-1}(\vec{y}-\vec{\mu}_{pr})\right], \\ \theta &\rightarrow \{\sigma, l\},\ K_{ij} = k(\rho_i,\rho_j) = \sigma \exp\left[\frac{(\rho_i-\rho_j)^2}{2l^2}\right], \end{aligned} \tag{A.3}$$

and the posterior as,

$$P(\vec{y}|\vec{d},\vec{\epsilon},\theta) = \frac{1}{(2\pi)^{\frac{n}{2}}\sqrt{|\Sigma_{post}|}} \exp\left[-\frac{1}{2}(\vec{y}-\mu_{post})^{\top}\Sigma_{post}^{-1}(\vec{y}-\mu_{post})\right]. \tag{A.4}$$

To derive μ_{post} and Σ_{post} the likelihood and prior are multiplied together and re-arranged. Only first and second order $\vec{y}$ terms are kept as the constants do not affect the shape of the multivariate Gaussian and thus do not affect μ_{post} or Σ_{post}. Then using the completing the square formula for matrices they can be combined into a single multivariate Gaussian. By comparing with the posterior we find the closed form expressions for μ_{post} and Σ_{post}. When the distributions are multiplied together the exponential powers are summed,

$$-\frac{1}{2}\left[(\vec{d}-R\vec{y})^\top\Sigma_{li}^{-1}(\vec{d}-R\vec{y})+(\vec{y}-\vec{\mu}_{pr})^\top K^{-1}(\vec{y}-\vec{\mu}_{pr})\right],$$

ignoring the $-\frac{1}{2}$ for now and multiplying it out gets,

$$\begin{aligned}\left(\vec{d}^\top\Sigma_{li}^{-1}\vec{d}-\vec{d}^\top\Sigma_{li}^{-1}R\vec{y}-(R\vec{y})^\top\Sigma_{li}^{-1}\vec{d}+(R\vec{y})^\top\Sigma_{li}^{-1}R\vec{y}\right),\\ +\left(\vec{y}^\top K^{-1}\vec{y}-\vec{y}^\top K^{-1}\vec{\mu}_{pr}-\vec{\mu}_{pr}^\top K^{-1}\vec{y}+\vec{\mu}_{pr}^\top K^{-1}\vec{\mu}_{pr}\right),\end{aligned}$$

focusing on the 1^{st} order terms and remembering that the transpose of a scalar is itself and the transpose of a symmetric matrix (e.g. Σ_{li}) is itself, it can be shown that the first order terms equate to

$$-\vec{d}^\top\Sigma_{li}^{-1}R\vec{y}-(R\vec{y})^\top\Sigma_{li}^{-1}\vec{d}-\vec{y}^\top K^{-1}\vec{\mu}_{pr}-\vec{\mu}_{pr}^\top K^{-1}\vec{y}=-2\vec{y}^\top(R^\top\Sigma_{li}^{-1}\vec{d}+K^{-1}\vec{\mu}_{pr})=-2\vec{y}^\top\vec{b}$$

in which a substitution was made to ease the use of the competing square formula,

$$\vec{b}=R^\top\Sigma_{li}^{-1}\vec{d}+K^{-1}\vec{\mu}_{pr}$$

switching the focus to the 2^{nd} order terms,

$$(R\vec{y})^\top\Sigma_{li}^{-1}R\vec{y}+\vec{y}^\top K^{-1}\vec{y}=\vec{y}^\top(R^\top\Sigma_{li}^{-1}R+K^{-1})\vec{y}=\vec{y}^\top M\vec{y},$$

in which a substitution was made to ease the use of the completing square formula,

$$M=(R^\top\Sigma_{li}^{-1}R+K^{-1})$$

ignoring 0 order terms that do not affect the shape, the original exponential power takes the form,

$$-\frac{1}{2}\left[\vec{y}^\top M\vec{y} - \vec{y}^\top\vec{b}\right],$$

by completing the squares we obtain

$$\vec{y}^\top M\vec{y} - y^\top\vec{b} = (\vec{y} - M^{-1}\vec{b})^\top M(\vec{y} - M^{-1}\vec{b}) - \vec{b}^\top M^{-1}\vec{b}.$$

We can ignore $\vec{b}^\top M^{-1}\vec{b}$ as it doesn't affect the shape of the Gaussian. Finally, for the posterior we have

$$P(\vec{y}|\vec{d},\vec{\epsilon},\theta) \propto \exp\left[-\frac{1}{2}(\vec{y} - \mu_{post})^\top\Sigma_{post}^{-1}(\vec{y} - \mu_{post})\right] \propto \exp\left[-\frac{1}{2}(\vec{y} - M^{-1}\vec{b})^\top M(\vec{y} - M^{-1}\vec{b})\right],$$

from comparison, it can be seen that,

$$\mu_{post} = M^{-1}\vec{b} = \left(R^\top\Sigma_{li}^{-1}R + K^{-1}\right)^{-1}\left(R^\top\Sigma_{li}^{-1}\vec{d} + K^{-1}\vec{\mu}_{pr}\right),\ \Sigma_{post} = M^{-1} = \left(R^\top\Sigma_{li}^{-1}R + K^{-1}\right)^{-1}. \tag{A.5}$$

The posterior mean is often written in another form. This form can be found with the following steps,

$$\begin{aligned}
\vec{\mu}_{post} &= (K^{-1} + R^\top\Sigma_{li}^{-1}R)^{-1}(R^\top\Sigma_{li}^{-1}\vec{d} + K^{-1}\vec{\mu}_{pr}) \\
&= (K^{-1} + R^\top\Sigma_{li}^{-1}R)^{-1}R^\top\Sigma_{li}^{-1}\vec{d} + (K^{-1} + R^\top\Sigma_{li}^{-1}R)^{-1}(K^{-1} + R^\top\Sigma_{li}^{-1}R - R^\top\Sigma_{li}^{-1}R)\vec{\mu}_{pr} \\
&= \vec{\mu}_{pr} + (K^{-1} + R^\top\Sigma_{li}^{-1}R)^{-1}R^\top\Sigma_{li}^{-1}\vec{d} - (K^{-1} + R^\top\Sigma_{li}^{-1}R)^{-1}R^\top\Sigma_{li}^{-1}R\vec{\mu}_{pr} \\
&= \vec{\mu}_{pr} + (K^{-1} + R^\top\Sigma_{li}^{-1}R)^{-1}R^\top\Sigma_{li}^{-1}(\vec{d} - R\vec{\mu}_{pr}).
\end{aligned}$$

The final closed form expression of the posterior mean and covariance is

$$\mu_{post} = \vec{\mu}_{pr} + (K^{-1} + R^\top\Sigma_{li}^{-1}R)^{-1}R^\top\Sigma_{li}^{-1}(\vec{d} - R\vec{\mu}_{pr}) \tag{A.6}$$

$$\Sigma_{post} = \left(R^\top\Sigma_{li}^{-1}R + K^{-1}\right)^{-1}. \tag{A.7}$$

The error of each value in μ_{post} can be found on the diagonal of Σ_{post}.

Appendix B

Deriving the Marginal Likelihood and Loss Function Expression

The marginal likelihood is the denominator in Bayes theorem for the inference

$$P(\vec{y}|\vec{d},\vec{\epsilon},\theta) = \frac{P(\vec{d}|\vec{y},\vec{\epsilon})P(\vec{y}|\theta)}{P(\vec{d}|\vec{\epsilon},\theta)}, \tag{B.1}$$

since the marginal likelihood is a normalizing constant it can be expressed as

$$P(\vec{d}|\vec{\epsilon},\theta) = \int P(\vec{d}|\vec{y},\vec{\epsilon})P(\vec{y}|\theta)\, d\vec{y}, \tag{B.2}$$

the likelihood is,

$$P(\vec{d}|\vec{y},\vec{\epsilon}) = \frac{1}{(2\pi)^{\frac{m}{2}}\sqrt{|\Sigma_{li}|}} \exp\left[-\frac{1}{2}(\vec{d}-R\vec{y})^\top \Sigma_{li}^{-1}(\vec{d}-R\vec{y})\right], \quad \Sigma_{li} = \vec{\epsilon}I, \tag{B.3}$$

and the prior is,

$$\begin{aligned} P(\vec{y}|\theta) &= \frac{1}{(2\pi)^{\frac{n}{2}}\sqrt{|K|}} \exp\left[-\frac{1}{2}(\vec{y}-\vec{\mu}_{pr})^\top K^{-1}(\vec{y}-\vec{\mu}_{pr})\right], \\ \theta \to \{\sigma, l\}, &\quad K_{ij} = k(\rho_i,\rho_j) = \sigma \exp\left[\frac{\rho_i-\rho_j}{2l^2}\right], \end{aligned} \tag{B.4}$$

when multiplied together the exponential powers become

$$\left(\vec{d}^\top \Sigma_{li}^{-1}\vec{d} - \vec{d}^\top \Sigma_{li}^{-1} R\vec{y} - (R\vec{y})^\top \Sigma_{li}^{-1}\vec{d} + (R\vec{y})^\top \Sigma_{li}^{-1} R\vec{y}\right) + \left(\vec{y}^\top K^{-1}\vec{y} - \vec{y}^\top K^{-1}\vec{\mu}_{pr} - \vec{\mu}_{pr}^\top K^{-1}\vec{y} + \vec{\mu}_{pr}^\top K^{-1}\vec{\mu}_{pr}\right),$$

the first order terms of $\vec{y}$ can be simplified,

$$-\vec{d}^\top \Sigma_{li}^{-1} R\vec{y} - (R\vec{y})^\top \Sigma_{li}^{-1}\vec{d} - \vec{y}^\top K^{-1}\vec{\mu}_{pr} - \vec{\mu}_{pr}^\top K^{-1}\vec{y} = -2\vec{y}^\top (R^\top \Sigma_{li}^{-1}\vec{d} + K^{-1}\vec{\mu}_{pr}) = -2\vec{y}^\top \vec{b},$$

the second order terms of $\vec{y}$ can be simplified,

$$(R\vec{y})^\top \Sigma_{li}^{-1} R\vec{y} + \vec{y}^\top K^{-1}\vec{y} = \vec{y}^\top (R^\top \Sigma_{li}^{-1} R + K^{-1})\vec{y} = \vec{y}^\top M\vec{y},$$

all together, for the marginal likelihood we have

$$\begin{aligned} P(\vec{d}|\vec{\epsilon},\theta) &= \int P(\vec{d}|\vec{y},\vec{\epsilon}) P(\vec{y}|\theta)\, d\vec{y} \\ &= \frac{1}{(2\pi)^{\frac{m}{2}}\sqrt{|\Sigma_{li}|}} \frac{1}{(2\pi)^{\frac{n}{2}}\sqrt{|K|}} \exp\left[-\frac{1}{2}(\vec{d}^\top \Sigma_{li}^{-1}\vec{d} + \vec{\mu}_{pr}^\top K^{-1}\vec{\mu}_{pr})\right] \int \exp\left[-\frac{1}{2}\vec{y}^\top M\vec{y} + \vec{y}^\top \vec{b}\right] d\vec{y}, \end{aligned} \tag{B.5}$$

performing a standard Gaussian integral we get that

$$\int \exp\left[-\frac{1}{2}\vec{y}^\top M\vec{y} + \vec{y}^\top \vec{b}\right] d\vec{y} = \frac{(2\pi)^{\frac{n}{2}}}{\sqrt{|M|}} \exp\left[\frac{1}{2}\vec{b}^\top M^{-1}\vec{b}\right],$$

all together, for the marginal likelihood we have

$$\begin{aligned} P(\vec{d}|\vec{\epsilon},\theta) &= \int P(\vec{d}|\vec{y},\vec{\epsilon}) P(\vec{y}|\theta)\, d\vec{y} \\ &= \frac{(2\pi)^{\frac{n}{2}}}{(2\pi)^{\frac{m}{2}}(2\pi)^{\frac{n}{2}}\sqrt{|\Sigma_{li}||K||M|}} \exp\left[-\frac{1}{2}(\vec{d}^\top \Sigma_{li}^{-1}\vec{d} + \vec{\mu}_{pr}^\top K^{-1}\vec{\mu}_{pr} - \vec{b}^\top M^{-1}\vec{b})\right], \end{aligned}$$

where $\vec{b}$ and M are substitutions made earlier

$$\vec{b} = R^\top \Sigma_{li}^{-1} \vec{d} + K^{-1} \vec{\mu}_{pr}$$
$$M = (R^\top \Sigma_{li}^{-1} R + K^{-1}),$$

ignoring the $-\frac{1}{2}$ for now and reverting $\vec{b}$ and M to their original form the exponential power becomes

$$\vec{\mu}_{pr}^\top K^{-1} \vec{\mu}_{pr} + \vec{d}^\top \Sigma_{li}^{-1} \vec{d} - (R^\top \Sigma_{li}^{-1} \vec{d} + K^{-1} \vec{\mu}_{pr})^\top (K^{-1} + R^\top \Sigma_{li}^{-1} R)^{-1} (R^\top \Sigma_{li}^{-1} \vec{d} + K^{-1} \vec{\mu}_{pr}),$$

the next step requires the Woodbury identity [8],

$$(A + UCV)^{-1} = A^{-1} - A^{-1} U (C^{-1} + V A^{-1} U)^{-1} V A^{-1}, \tag{B.6}$$

the exponential power can thus be expanded to be

$$\vec{\mu}_{pr}^\top K^{-1} \vec{\mu}_{pr} + \vec{d}^\top \Sigma_{li}^{-1} \vec{d} - (R^\top \Sigma_{li}^{-1} \vec{d} + K^{-1} \vec{\mu}_{pr})^\top \left[K - K R^\top \left(\Sigma_{li} + R K R^\top \right)^{-1} R K \right] (R^\top \Sigma_{li}^{-1} \vec{d} + K^{-1} \vec{\mu}_{pr}),$$

This can then be rearranged to be

$$\begin{aligned} \vec{d}^\top \left\{ \Sigma_{li}^{-1} - \Sigma_{li}^{-1} R \left[K - K R^\top \left(\Sigma_{li} + R K R^\top \right)^{-1} R K \right] R^\top \Sigma_{li}^{-1} \right\} \vec{d} \\ - 2 \vec{\mu}^\top K^{-1} \left[K - K R^\top \left(\Sigma_{li} + R K R^\top \right)^{-1} R K \right] R^\top \Sigma_{li}^{-1} \vec{d} \\ + \vec{\mu}^\top \left\{ K^{-1} - K^{-1} \left[K - K R^\top \left(\Sigma_{li} + R K R^\top \right)^{-1} R K \right] K^{-1} \right\} \vec{\mu}, \end{aligned}$$

the second order term in $\vec{d}$ can be reduced

$$\begin{aligned} \Sigma_{li}^{-1} - \Sigma_{li}^{-1} R \left[K - K R^\top \left(\Sigma_{li} + R K R^\top \right)^{-1} R K \right] R^\top \Sigma_{li}^{-1} \\ &= \Sigma_{li}^{-1} - \Sigma_{li}^{-1} R K R^\top \Sigma_{li}^{-1} + \Sigma_{li}^{-1} R K R^\top \left(\Sigma_{li} + R K R^\top \right)^{-1} R K R^\top \Sigma_{li}^{-1} \\ &= \Sigma_{li}^{-1} - \Sigma_{li}^{-1} R K R^\top \Sigma_{li}^{-1} + \Sigma_{li}^{-1} \left(\Sigma_{li} + R K R^\top - \Sigma_{li} \right) \left(\Sigma_{li} + R K R^\top \right)^{-1} R K R^\top \Sigma_{li}^{-1} \\ &= \Sigma_{li}^{-1} - \left(\Sigma_{li} + R K R^\top \right)^{-1} R K R^\top \Sigma_{li}^{-1} \\ &= \Sigma_{li}^{-1} - \left(\Sigma_{li} + R K R^\top \right)^{-1} \left(\Sigma_{li} + R K R^\top - \Sigma_{li} \right) \Sigma_{li}^{-1} \\ &= \left(\Sigma_{li} + R K R^\top \right)^{-1}, \end{aligned}$$

the first order term in $\vec{d}$ can be reduced

$$\begin{aligned}
-2\vec{\mu}^\top K^{-1}&\left[K - KR^\top\left(\Sigma_{li} + RKR^\top\right)^{-1}RK\right]R^\top\Sigma_{li}^{-1}\\
&= -2\vec{\mu}^\top R^\top\Sigma_{li}^{-1} + 2\vec{\mu}^\top R^\top\left(\Sigma_{li} + RKR^\top\right)^{-1}RKR^\top\Sigma_{li}^{-1}\\
&= -2\vec{\mu}^\top R^\top\Sigma_{li}^{-1} + 2\vec{\mu}^\top R^\top\left(\Sigma_{li} + RKR^\top\right)^{-1}\left(\Sigma_{li} + RKR^\top - \Sigma_{li}\right)\Sigma_{li}^{-1}\\
&= -2\vec{\mu}^\top R^\top\Sigma_{li}^{-1} + 2\vec{\mu}^\top R^\top\Sigma_{li}^{-1} - 2\vec{\mu}^\top R^\top\left(\Sigma_{li} + RKR^\top\right)^{-1}\\
&= -2\vec{\mu}^\top R^\top\left(\Sigma_{li} + RKR^\top\right)^{-1},
\end{aligned}$$

the zero order term in $\vec{d}$ can be reduced

$$K^{-1} - K^{-1}\left[K - KR^\top\left(\Sigma_{li} + RKR^\top\right)^{-1}RK\right]K^{-1} = R^\top\left(\Sigma_{li} + RKR^\top\right)^{-1}R,$$

now the exponential is

$$\begin{aligned}
&\vec{d}^\top\Sigma_{li}^{-1}\vec{d} + \vec{\mu}_{pr}^\top K^{-1}\vec{\mu}_{pr} - \vec{b}^\top M^{-1}\vec{b}\\
&\qquad= \vec{d}^\top\left(\Sigma_{li} + RKR^\top\right)^{-1}\vec{d} - 2\vec{\mu}^\top R^\top\left(\Sigma_{li} + RKR^\top\right)^{-1} + \vec{\mu}^\top R^\top\left(\Sigma_{li} + RKR^\top\right)^{-1}R\vec{\mu}\\
&\qquad= (\vec{d} - R\vec{\mu}_{pr})^\top(\Sigma_{li} + RKR^\top)^{-1}(\vec{d} - R\vec{\mu}_{pr}),
\end{aligned}$$

the scaling constant can be simplified using the matrix determinant lemma [8],

$$|A + UCV| = |A|\,|C|\,|C^{-1} + VA^{-1}U|, \tag{B.7}$$

$$|\Sigma_{li}||K||M| = |\Sigma_{li}||K||R^\top\Sigma_{li}^{-1}R + K^{-1}| = |\Sigma_{li} + RKR^\top|,$$

this also helps avoid precision errors as there are fewer matrix inversions and determinants to compute. The marginal likelihood becomes

$$\begin{aligned}
P(\vec{d}|\vec{\epsilon},\theta) &= \int P(\vec{d}|\vec{y},\vec{\epsilon})P(\vec{y}|\theta)\,d\vec{y}\\
&= \frac{1}{(2\pi)^{\frac{m}{2}}\sqrt{|\Sigma_{li} + RKR^\top|}}\exp\left[-\frac{1}{2}(\vec{d} - R\vec{\mu}_{pr})^\top(\Sigma_{li} + RKR^\top)^{-1}(\vec{d} - R\vec{\mu}_{pr})\right].
\end{aligned} \tag{B.8}$$

The values of the marginal likelihood can become very large and troublesome to compute with standard 64-bit float precision. For this reason, the logarithm is computed,

$$\ln(P(\vec{d}|\vec{\epsilon},\theta)) = -\frac{1}{2}\left[m\ln(2\pi) + \ln(|\Sigma_{li} + RKR^\top|) + (\vec{d} - R\vec{\mu}_{pr})^\top(\Sigma_{li} + RKR^\top)^{-1}(\vec{d} - R\vec{\mu}_{pr})\right]. \tag{B.9}$$

It is convention for loss functions to be minimized so the negative log marginal likelihood is used as the loss function for optimizing the hyper-parameters. When minimizing, the constants do not play a major role, thus the loss function for the hyperparameters is expressed as

$$loss(\epsilon,\theta) = \ln(|\Sigma_{li} + RKR^\top|) + (\vec{d} - R\vec{\mu}_{pr})^\top(\Sigma_{li} + RKR^\top)^{-1}(\vec{d} - R\vec{\mu}_{pr}) \tag{B.10}$$

Appendix C

Complete Set of Distributions and Expressions for Reference

C.1 Gaussian Process Regression for Interferometry, Discluding Artificial Observations

In section 2.3, Gaussian process regression was introduced for a simple regression problem. In section 2.5 it was explained how to alter GPR so that it could be applied to interferometry. Here are the mentioned distributions fully described for reference. The likelihood is,

$$\begin{aligned}\mathcal{N}(\vec{d}, \vec{\mu_{li}} = R\vec{n_e}, \Sigma_{li}) &= \frac{1}{\sqrt{(2\pi)^{\frac{n}{2}}|\Sigma_{li}|}} \exp\left[-\frac{1}{2}(\vec{d} - R\vec{n_e})^\top \Sigma_{li}^{-1}(\vec{d} - R\vec{n_e})\right], \\ \Sigma_{li} = \vec{\epsilon} I &= \begin{bmatrix} \epsilon_1 & 0 & \cdots & 0 \\ 0 & \epsilon_2 & \cdots & 0 \\ \vdots & \vdots & \ddots & 0 \\ 0 & 0 & 0 & \epsilon_m \end{bmatrix},\end{aligned} \tag{C.1}$$

where R is a matrix composed of flux surface contribution row vectors, where each row vector corresponds to a different line of sight and when multiplied with $\vec{n_e}$ produces the line integrated density over that line of sight, see section 2.5 for more details. The prior is,

$$\mathcal{N}(\vec{n_e}, \vec{\mu}_{pr} = \vec{0}, K) = \frac{1}{\sqrt{(2\pi)^{\frac{n}{2}}|K|}} \exp\left[-\frac{1}{2}\vec{n_e}^{\top} K^{-1} \vec{n_e}\right],$$
$$K_{ij} = k(\rho_i, \rho_j) = \sigma^2 \left(\frac{2l(\rho_i)l(\rho_j)}{l(\rho_i)^2 + l(\rho_j)^2}\right)^{1/2} \exp\left(\frac{(\rho_i - \rho_j)^2}{l(\rho_i)^2 + l(\rho_j)^2}\right), \tag{C.2}$$

where $l(\rho)$ can be a hyperbolic tangent function or otherwise. If l is not a function but a constant, $l(\rho) = l$, then the kernel reverts back to the static kernel,

$$K_{ij} = k(\rho_i, \rho_j) = \sigma \exp\left[\frac{\rho_i - \rho_j}{2l^2}\right], \tag{C.3}$$

The goal is to compute the posterior,

$$\mathcal{N}(\vec{n_e}, \vec{\mu_{post}}, \Sigma_{post}) = \frac{1}{\sqrt{(2\pi)^{\frac{n}{2}}|\Sigma_{post}|}} \exp\left[-\frac{1}{2}(\vec{n_e} - \mu_{post})^{\top} \Sigma_{post}^{-1} (\vec{n_e} - \mu_{post})\right], \tag{C.4}$$

which can be done with the closed form expressions,

$$\mu_{post} = \vec{\mu}_{pr} + (K^{-1} + R^{\top}\Sigma_{li}^{-1}R)^{-1} R^{\top}\Sigma_{li}^{-1}(\vec{d} - R\vec{\mu}_{pr}) \tag{C.5}$$
$$\Sigma_{post} = \left(R^{\top}\Sigma_{li}^{-1}R + K^{-1}\right)^{-1}. \tag{C.6}$$

as derived in appendix A. Once known the density profile can be plotted with the $\vec{\mu_{post}}$ values at the same ρ values used in the kernel. The errors are the standard deviations held in the diagonal of Σ_{post}. This calculation is unlikely to be accurate until the hyperparameters are optimised. The parameters in the length scale function $l(\rho)$ are hyperparameters. The experimental errors ϵ can also be hyperparameters if unknown. The optimal hyperparameters can be found by minimising the negative log marginal likelihood. It is derived in appendix B to be,

$$-\ln(P(\vec{d}|\vec{\epsilon}, \theta)) \propto \ln(|\Sigma_{li} + RKR^{\top}|) + (\vec{d} - R\vec{\mu}_{pr})^{\top}(\Sigma_{li} + RKR^{\top})^{-1}(\vec{d} - R\vec{\mu}_{pr}). \tag{C.7}$$

There is no change in its form from the simple regression problem. The values of the various matrices and vectors have changed.

C.2 Gaussian Process Regression for Interferometry, Including Artificial Observations

Artificial observations can be placed in the likelihood to include prior knowledge. This circumvents precision issues when including this information in the prior. The process was explained in section 2.5. Here are the full expressions for reference. The likelihood is,

$$
\begin{aligned}
&\mathcal{N}(\vec{d^{alt}}, \vec{\mu_{li}} = R^{alt}\vec{a}, \Sigma_{li}) = \frac{1}{\sqrt{(2\pi)^{\frac{n}{2}}|\Sigma_{li}^{alt}|}} \exp\left[-\frac{1}{2}(\vec{d^{alt}} - R^{alt}\vec{a})^{\top}(\Sigma_{li}^{alt})^{-1}(\vec{d} - R^{alt}\vec{a})\right], \\
&\vec{d}^{alt} = \begin{bmatrix} \vec{d} \\ n_e(\rho=1)=0 \\ n_e'(\rho=0)=0 \end{bmatrix} = \begin{bmatrix} lid_1 \\ lid_2 \\ \vdots \\ lid_m \\ n_e(\rho=1)=0 \\ n_e'(\rho=0)=0 \end{bmatrix}, \\
&\vec{a} = \begin{bmatrix} \vec{n_e} \\ n_e(\rho=1) \\ n_e'(\rho=0) \end{bmatrix} = \begin{bmatrix} n_e(\rho_1) \\ n_e(\rho_2) \\ \vdots \\ n_e(\rho_n) \\ n_e(\rho=1) \\ n_e'(\rho=0) \end{bmatrix}, \\
&\Sigma_{li}^{alt} = I \begin{bmatrix} \vec{\epsilon} \\ \epsilon_{edge} \\ \epsilon_{core}' \end{bmatrix} = I \begin{bmatrix} \epsilon_1 \\ \epsilon_2 \\ \vdots \\ \epsilon_m \\ \epsilon_{edge} \\ \epsilon_{core}' \end{bmatrix} = \begin{bmatrix} \epsilon_1 & 0 & \cdots & 0 & 0 & 0 \\ 0 & \epsilon_2 & \cdots & 0 & 0 & 0 \\ \vdots & \vdots & \ddots & 0 & 0 & 0 \\ 0 & 0 & 0 & \epsilon_m & 0 & 0 \\ 0 & 0 & 0 & 0 & \epsilon_{edge} & 0 \\ 0 & 0 & 0 & 0 & 0 & \epsilon_{core}' \end{bmatrix}, \\
&R^{alt} = \begin{bmatrix} R & \cdots & 0 & 0 \\ \vdots & \ddots & 0 & 0 \\ 0 & 0 & 1 & 0 \\ 0 & 0 & 0 & 1 \end{bmatrix},
\end{aligned}
\tag{C.8}
$$

where $\vec{d}$ has been altered to include the data from the artificial observations, lid_1 is the line integrated density from the 1^{st} laser of m lasers. $\vec{a}$ is the vector to be inferred and is the original electron density profile $\vec{n_e}$ with the additional artificial observations, $\vec{\epsilon}$ contains the experimental errors of the interferometry for each line of sight and ϵ_{edge} is the error of our artificial observation for the electron density at the edge, it represents the strength of our prior assumption. ϵ'_{core} represents the error of the artificial observation that the density gradient is 0 at the core, it also represents the strength of this prior assumption. R is the original response matrix explained previously and R^{alt} is a small alteration to return the artificial observations when applied to some $\vec{a}$. The prior is,

$$\begin{aligned}
&\mathcal{N}(\vec{a}, \vec{\mu}_{pr} = \vec{0}, K^{alt}) = \frac{1}{\sqrt{(2\pi)^{\frac{n}{2}}|K^{alt}|}} \exp\left[-\frac{1}{2}\vec{a}^{\top}(K^{alt})^{-1}\vec{a}\right], \\
&K^{alt} = \begin{bmatrix} K & K' \\ -K'^{\top} & K'' \end{bmatrix}, \\
&K_{ij} = k(\rho_i, \rho_j) = \sigma^2 \left(\frac{2l(\rho_i)l(\rho_j)}{l(\rho_i)^2 + l(\rho_j)^2}\right)^{1/2} \exp\left(\frac{(\rho_i - \rho_j)^2}{l(\rho_i)^2 + l(\rho_j)^2}\right), \\
&K'_{ij} = k'(\rho'_i, \rho_j) = \frac{\partial k(\rho'_i, \rho_j)}{\partial \rho'_i}, \\
&K''_{ij} = k''(\rho'_i, \rho'_j) = \frac{\partial k(\rho'_i, \rho'_j)}{\partial \rho'_i \partial \rho'_j},
\end{aligned} \tag{C.9}$$

where $l(\rho)$ can be a hyperbolic tangent function or otherwise. If $l(\rho) = l$ then this reverts to the static kernel,

$$K_{ij} = k(\rho_i, \rho_j) = \sigma \exp\left[\frac{\rho_i - \rho_j}{2l^2}\right]. \tag{C.10}$$

The K' and K'' are required to account for the fact that now there is gradient information and the covariance for positions of gradient information ρ' requires a differential of the original covariance kernel k. The goal is to compute the posterior,

$$\mathcal{N}(\vec{a}, \vec{\mu_{post}}, \Sigma_{post}) = \frac{1}{\sqrt{(2\pi)^{\frac{n}{2}}|\Sigma_{post}|}} \exp\left[-\frac{1}{2}(\vec{a} - \mu_{post})^{\top}\Sigma_{post}^{-1}(\vec{a} - \mu_{post})\right], \tag{C.11}$$

where since $\vec{n_e}$ has been extended to $\vec{a}$ the $\vec{\mu}_{post}$ and Σ_{post} have also been extended. The careful choice of alterations allows us to use the same closed form expressions as before the

artificial observations simply by inserting the alternate forms of the various matrices and vectors. The marginal likelihood for optimization also holds its form. To get the density profile one must remove the end terms of μ_{post} associated with the artificial observations before plotting. The same applies to the diagonal of Σ_{post} to obtain the errors.

Glossary

GPR Gaussian Process Regression is a method of performing inference on continuous values using a Gaussian process prior. A Gaussian process is a collection of random variables that have a joint multivariate normal distribution. A Gaussian process can be completely defined by its mean function and covariance function, which specify the expected value and the correlation of any finite subset of variables. Gaussian process regression uses the observed data to update the prior distribution and obtain a posterior distribution, which can be used to make predictions and estimate the uncertainty of the results. 2, 6, 8, 9, 11, 14, 17–19, 34

IMAS Integrated Modeling and Analysis Suite, is a framework and data management system. It is designed to store, manage, and analyze experimental and simulation data. IMAS provides a standardized platform for sharing and exchanging data among researchers from different institutions and countries. IMAS supports the integration of various fusion modeling codes and allows researchers to compare experimental data with simulation results. 6, 13

MHD MHD stands for magnetohydrodynamics. It is a model of electrically conducting fluids that treats all interpenetrating particle species together as a single continuous medium. It is primarily concerned with the low-frequency, large-scale, magnetic behavior in plasmas and liquid metals. 4

NICE Newton direct and Inverse Computation for Equilibrium. A code developed by Blaise Faugeras at the Centre national de la recherche scientifique (CNRS) to numerically solve several plasma free-boundary equilibrium problems within a tokamak including the position of magnetic flux surfaces and the electron density profile. 1, 2, 4–6, 14, 19

SQP Sequential Quadratic Programming is a numerical optimization technique used to solve nonlinear constrained optimization problems. It is an iterative method that seeks to find the optimal solution to a problem by iteratively approximating it with a quadratic model and then solving this quadratic subproblem. The key idea is to successively update the solution in a way that moves closer to the optimal solution while satisfying the constraints. 6

WEST **Tungsten** (W) Environment in Steady-state Tokamak (WEST) is a French tokamak that aims to test and validate the ITER tungsten divertor components and prepare their safe operation 1, 5, 6, 13, 14, 17, 19